AIAA 2005-7066

Integration of an Autopilot for a Micro Air Vehicle

George Platanitis* and Sergey Shkarayev.†
University of Arizona, Tucson, AZ, 85721-0119

The integration of a commercially available autopilot, the MicroPilot MP2028^g, is investigated for a 36-inch Zagi airframe. Analytical methods, including the Advanced Aircraft Analysis software from DARCorp, were used to determine the stability and control derivatives, and then validated through wind tunnel experiments. From this data, the linear, perturbed model about steady-state flight conditions was cast and transfer functions for the control and navigation systems were developed. Feedback control laws based on Proportional, Integral, and Derivative (PID) control design were developed to control the aircraft which may then be programmed into the autopilot. Flight tests were performed in remote control mode to evaluate handling, adjust trim, and test data logging for the Zagi with integrated MP2028^g. Ground testing was performed to test GPS acquisition, data logging, and control response in autonomous mode. Technical difficulties and integration limitations with the autopilot prevented fully autonomous flight from taking place, but the integration methodologies are, in general, applicable for unmanned air vehicles that use a PID control based autopilot.

Nomenclature

C_{D_min} = zero angle-of-attack drag
C_{D1} = steady state drag
C_{D*} = drag coefficient derivatives
C_{L1} = steady state lift
C_{Lwo} = zero angle-of-attack lift coefficient
C_{L*} = lift coefficient derivatives
C_{M1} = steady state moment coefficient
C_{Mwo} = zero angle-of-attack moment coefficient
C_{M*} = moment coefficient derivatives
C_{mu} = moment stability derivative coefficient due to airspeed
C_{xu} = drag stability derivative coefficient due to airspeed
$C_{x\alpha}$ = drag stability derivative coefficient due to angle-of-attack
C_{zu} = lift stability derivative coefficient due to airspeed
$C_{z\alpha}$ = lift stability derivative coefficient due to angle-of-attack
$C_{y\beta}$ = side force stability derivative coefficient due to sideslip angle
C_{l*} = rolling moment stability derivative coefficients
C_{n*} = yaw moment stability derivatives coefficients
g = acceleration due to gravity
$G(s)$ = Laplace transform of system dynamics
h , $\dot{h}$ = altitude, rate of change of altitude
I_{**} = mass moment of inertia, body roll, pitch, and yaw axis
I_{xz} = body x-z product inertia
r = reference input
u = perturbed airspeed
$u(t)$ = control input
U_o = steady state airspeed
y = output response
γ = flight path angle
x_{ac} = aerodynamic center measured from wing apex
x_{cg} = center-of-gravity location measured from wing apex
α = angle-of-attack
β = sideslip angle
δ_a = aileron deflection
δ_e = elevator deflection
θ = pitch attitude
ϕ = bank angle
ψ = heading angle

* Post-Doctoral Research Associate, Department of Aerospace and Mechanical Engineering, PO Box 210119, 1130 N. Mountain Ave., Tucson, AZ, 85721. AIAA Member.
† Associate Professor, Department of Aerospace and Mechanical Engineering, PO Box 210119, 1130 N. Mountain Ave., Tucson, AZ, 85721. AIAA Associate Member.

I. Introduction

Micro Air Vehicle research has been a topic of interest in recent years. In 1996, the Defense Advanced Research Projects Agency (DARPA) initiated the broad-based program on micro air vehicle research and development.[1] Applications of small, unmanned aircraft range from both military to scientific, and their versatility allows them to perform in conditions that might otherwise endanger human life. In several papers,[2,3,4] Micro Air Vehicle research at the University of Arizona has been presented. Here, investigations took place into the design of an adaptive wing structure, where several camber configurations (3, 6, 9, and 12 percent) of a thin, cambered plate airfoil based on the S5010-TOP24C-REF airfoil were investigated. Wind tunnel data was gathered for the lift, drag, and moment at several angles of attack over a range of freestream velocities (corresponding to associated chord Reynolds numbers). The lift-to-drag ratios were also determined and insight into optimal camber configurations were realized for various flight conditions to give best performance at both high and low flight speeds.

Flexible wing micro air vehicles have been investigated in papers by Waszak, et al.,[5] and Ifju, et al.[6] In the investigations, wing frames of varying material compositions for the wing membrane and batten arrangements of carbon fiber skeletons were constructed to provide a range of flexibilities. Their aerodynamic properties were investigated in wind tunnel experiments. The authors found that higher angles of attack may be achieved without stalling using a flexible wing that deforms under varying aerodynamic loads, including gust conditions, allowing the wing to see a lower angle of attack at higher pitch attitudes. Also, streamlining the fuselage of the MAV improved the lift-to-drag ratio on the aircraft, resulting in better overall performance. Ongoing investigations in the stability and control of the MAVs are also taking place. An analysis of the static stability derivatives shows the aircraft to be stable in all axes, where the nondimensional stability derivatives were found to be generally larger than conventional, piloted aircraft.[6]

A major topic of interest in this research is in methods of developing a system for autonomous flight of an MAV. In Foster, et al.,[7] the dynamic stability of several small unmanned air vehicles (UAV) is analyzed using predictive software programs. Based on these results, handling quality guidelines are proposed using scaled-down standards from standards used for larger aircraft. Thus, new short-period natural frequency standards for small UAVs may be established. In Hsiao, et al.,[8] a low cost system with an auto-lockup Charge-Coupled Device (CCD) was developed for autonomous flight and image capturing. The onboard system measures aircraft attitude, height, 3-D position via a GPS receiver, and collects data from the air data sensor and dynamic measuring unit, transmitting them to a PC-based onboard computer. An algorithm then calculates the target position for a gimbaled CCD camera, allowing real-time images to be transmitted to a ground station. Flight control was also investigated in Arning, et al.[9] The potential of using micro electromechanical systems (MEMS) technology to provide size and weight savings, along with reduced power consumption for autopilot hardware mounted on the MAV is realized. Successful flight tests were carried out on both fixed-wing and rotary-wing MAVs. In Taylor, et al.,[10] an attitude stabilization system based on thermal horizon detection was developed. The system operates in Visual Meteorological Conditions (VMC), is reliable in daytime or nighttime flight, consumes little power, and operates quickly from a cold start. Such a control system even allows a non-pilot the ability to fly a UAV, while giving more attention to his own projects. Finally, the ability to control MAVs is treated in Ref. 11. MEMS technology is discussed for improving MAV performance, while the rest of the paper focuses on improving airfoil design for better lift-to-drag characteristics. MEMS sensing and actuation may be used to delay or prevent flow separation better, compared to traditional flow control and over traditional mechanical control surfaces. Also, chaotic mixing may be used to delay laminar separation. Genetic algorithms may be used in conjunction with Navier-Stokes algorithms to aid in determining an optimum profile for the design of an MAV lifting surface.

The 8th International Micro Air Vehicle Competition has showcased two designs of MAVs that demonstrated aircraft flight via an autopilot. In Ref. 12, the design team from Brigham Young University developed their aircraft through an iterative process, which involved a stability analysis of the five aircraft modes (phugoid, short period, dutch-roll, roll, and spiral), until it met functional specifications from various industry organizations. Implementation of the MAGICC autopilot provided reliable hands-off control, with capabilities that are competitive with larger UAVs, and the design was shown to be economically competitive with the most economical UAVs that are commercially available. Another entrant[13] developed a control system for autonomous flight of an MAV for the surveillance mission of the competition. Here, an existing autopilot system was modified by the augmentation of a GPS-receiver and telemetry system which uses a waypoint navigation algorithm. Newly developed control laws

were integrated into a ground station, allowing gain factors and waypoints to be modified during flight. The system developed is more flexible and the MAV can navigate pilot-independent along GPS waypoints.

At the 9th International Micro Air Vehicle Competition, a team from Konkuk University[14] made improvements in the flight ability of their MAV entry, and selected components for their MAV for surveillance and endurance missions. A micro-scale inertial measurement system, the MR01, was developed for the micro-scale autopilot system. The MR01 consists of a one-axis gyroscope sensor, and a two-axis accelerometer. When attitude data measured by the MR01 was used as feedback for the servomotor control, longitudinal and lateral stabilities improved. Successful missions have been flown using 13-15 cm wing span MAVs for surveillance in 5 m/s headwinds.

Recently, an autopilot system using the U-NAV Pico-Pilot for the navigation system[15] was tested on a 12-inch MAV, a robust aircraft serving as a baseline design for the research and development program initiated during the summer of 2004 at the University of Arizona. A FMA Co-Pilot system was integrated with the Pico-Pilot to work parallel to the navigation system. It uses four infra-red sensors to obtain information about the aircraft's attitude and orientation relative to the ground, feeding back this information to the stability system. An elevator and dorsal rudder are deflected as required to maintain level flight. GPS navigation was used to guide the aircraft to points along a preprogrammed flight path. The autopilot system navigated the aircraft through complex courses with excellent accuracy and repeatability, with wind speeds up to 20 mph. The Co-Pilot has shown some problems with control authority in the roll and pitch, causing the aircraft to oscillate in these directions. However, the aircraft still maintained its heading, following the prescribed course.

This paper focuses on the integration of an autopilot system, the MP2028^g, for a 36-inch Zagi MAV. The aircraft provides a useful platform for evaluating autopilot integration into MAVs of comparable size. The MP2028^g is a commercially available autopilot system that has been successfully used on large unmanned air vehicles, yet little is known as to how feasible integration of this autopilot system is on smaller vehicles. The autopilot allows the user to program a control law onto the onboard processor, as well as mission information. The aircraft would then fly the given mission autonomously (including take-off and landing). The autopilot uses various feedback loops for navigation and control during autonomous flight. While one may use empirical approaches (set gains and flight test) to determine appropriate gains, the motivation of this research is to provide a more systematic approach to determining feedback loop gains. The approach involves determining an analytical model of the aircraft from its structural and aerodynamic characteristics that can then be validated through wind tunnel experiments, and developing the feedback control loops using standard design methods. Flight testing would follow to evaluate control designs. Much of the paper is devoted to the Zagi's operation, with integration of the MP2028^g to provide autonomous flight capabilities and developing methods to systematically determine appropriate control gains for the autopilot to provide stable flight.

II. Zagi MAV Background

Zagis have often been used as training aircraft for beginners in remote control flight.[16] The Zagi MAV used for this research is a Styrofoam, tailless aircraft configuration with physical properties described in Table 1. A Kevlar base and carbon rods reinforce the airframe. Balsawood is used for the control surfaces, in an elevon configuration, and are actuated by servomotors, with a deflection range of ±30 degrees. The wing uses a Martin Hepperle MH45 airfoil cross section. Plastic winglets assist in reducing aerodynamic drag and provide some limited lateral-directional stability. Lift, drag, and moment data for the airfoil are readily available[17] and aerodynamic characteristics were calculated using methods described in Ref. 18 and 19. A rear-mounted Rotex 25/6/15 motor with an attached propeller provides thrust. The motor is rear-mounted to eliminate aerodynamic effects due to the spinning propeller. Power is provided by a Polyquest PQ-B1100-HG3S lithium-polymer battery, rated at 11.1 V and 1100 mAh. In the present study, the aerodynamic properties of the Zagi MAV were also determined through wind tunnel experiments.

Figure 1. Views of the 36" Zagi.

Table 1: Physical properties of Zagi MAV.

Parameter	Value	Parameter	Value
Span	0.926 m	Total mass	0.4309 kg
Wing tip chord	0.120 m	I_{xx}	0.02045 kg.m^2
Wing root chord	0.2850 m	I_{yy}	0.004739 kg.m^2
Taper ratio	0.4211	I_{zz}	0.02515 kg.m^2
Wing area	0.1875 m^2	I_{xz}	2.974 x 10^{-5} kg.m^2
Quarter-chord wing sweep	34.69°	Oswald efficiency factor	0.7854
Aspect ratio	4.5728	Fuselage length	0.216 m
x_{cg} *	0.18 m	Fuselage max. width	0.187 m
x_{ac} *	0.2097 m	Fuselage max. height	0.052 m

*measured from aircraft nose (coincides with wing apex).

A. Aerodynamic Model of 36-inch Zagi

There are several methods that allow one to produce an aircraft model. One is through the use of analytical software, such as DARCorp's Advanced Aircraft Analysis (AAA),[20] a widely used software tool by aircraft designers. There are ten modules in the software, including one for aerodynamic characteristics, and another for determining stability and control derivatives. At the same time, the aerodynamic data from wind tunnel experiments may be used to obtain stability and control derivatives in order to validate computed values. In the present study, the airfoil data was used as one of the inputs to AAA for the determination of the aerodynamic characteristics of the Zagi. Table 2 summarizes the aerodynamic parameters determined using AAA software for the low flight speed range. These results provide an approximation of the flight characteristics from which a model of the aircraft can be derived.

The stability and control derivatives are determined by differentiating the force and moment equations with respect to each perturbed variable of motion (perturbed velocity, angle-of-attack, pitch rate, etc.) and the linear, perturbed equations of motion from steady-state are cast in terms of these derivatives. These stability and control derivatives are important in efficient system design and represent the acceleration per unit change of their associated motion or control variable. Their numerical values give an indication of their relative importance. From the linear equations of motion, six principal transfer functions are determined. The three longitudinal transfer functions will have an elevator input, with perturbed velocity, angle of attack, and pitch as outputs. The three lateral-directional derivatives will have an aileron input, with perturbed sideslip angle, bank angle, and heading angle as outputs. Closed-loop control laws may be designed from these transfer functions using standard control analysis.

Table 2: Aerodynamic data for the Zagi MAV.

Longitudinal		Lateral	
Parameter	Value	Parameter	Value
C_{D_min}	0.01631	$C_{y\beta}$	-0.07359
C_{D1}	0.02228	$C_{l\beta}$	-0.02854
$C_{D\alpha}$	0.2108	C_{lp}	-0.3209
$C_{D\delta e}$	0.3045	C_{lr}	0.03066
C_{Lu}	0.0004469	$C_{l\delta a}$	0.1682
C_{Lwo}	0.09167	$C_{n\beta}$	-0.0004012
C_{L1}	0.3964	C_{np}	-0.01297
$C_{L\alpha}$	3.5016	C_{nr}	-0.004337
C_{Lq}	2.8932	$C_{n\delta a}$	-0.003281
$C_{L\delta e}$	0.2724	$C_{M\alpha}$	-0.5675
C_{Mu}	-1.693×10^{-5}	C_{Mq}	-1.3990
C_{Mwo}	-0.02338	$C_{M\delta e}$	-0.3254
C_{M1}	-0.03489	C_{mu}	$C_{Mu} + 2C_{M1}$
C_{xu}	$C_{Du} + 2C_{D1}$	C_{zu}	$C_{Lu} + 2C_{L1}$
$C_{x\alpha}$	$C_{D\alpha} - C_{L1}$	$C_{z\alpha}$	$C_{L\alpha} + C_{D1}$

B. Wind Tunnel Experiments

In order to provide validation for the use of the predicted aerodynamic data, wind tunnel measurements were made using a scaled-down model of the Zagi (at half-sized dimensions), built as a wing-only model. The actual aircraft also has a small fuselage cap to protect the autopilot hardware and electronics and its aerodynamic influence was assumed negligible. Experiments were conducted in the 4' x 3' low-speed wind tunnel[4,21] at the University of Arizona. As only the longitudinal strain gauges were functional, only longitudinal loads could be measured. Aerodynamic data was collected for the model aircraft at a wind tunnel speed of 17.8 m/s (mean chord Reynolds number of 1.21×10^5, equivalent to the actual aircraft flying at approximately 9 m/s). At this condition, low-speed aerodynamic characteristics may be validated. The model aircraft's angle of attack and control surface deflection were varied and aerodynamic forces and moments were measured. Tares were taken for the mounting pylon and the aerodynamic influence of the pylon was subtracted from the total loads measured. This way, only the loads on the aircraft remain. The 36-inch Zagi is not expected to fly faster than ~20 m/s, a velocity range where the low-speed aerodynamic coefficients change very little.

Table 3 summarizes the aerodynamic lift and drag coefficients and coefficient derivatives for angle of attack and control surface deflection, and compares them against predicted values from the AAA software. Only the coefficient derivative for lift versus angle-of-attack could be determined accurately from the experiment. The large errors between the measured and predicted values of the aerodynamic coefficients clearly show that refinements in the experimental procedure are needed. Coefficients that are generally small (such as the drag coefficients and zero angle-of-attack coefficients) will show a high level of sensitivity to measurement error, a consequence of the somewhat crude experimental setup. Also, the control surfaces are not of a typical size (~16 percent of the mean chord, whereas conventional size can be as much as 30 percent), making it difficult to measure their aerodynamic characteristics. Since the wind tunnel model aircraft did not have any means of locking the control surfaces at a desired deflection, the control surfaces would experience flexibility effects at the joints caused by the dynamic pressure influence.

Table 3: Experimental aerodynamic coefficients for the Zagi MAV for longitudinal forces compared against predicted values.

Parameter	Experimental Value	Predicted Value	% Error |Exp. – Pred.|/Pred.
C_{D_min}	0.02812	0.01631	72
$C_{D\alpha}$	0.07245	0.2108	66
$C_{D\delta e}$	0.009368	0.3045	97
C_{Lwo}	0.1696	0.09167	85
$C_{L\alpha}$	3.5722	3.5016	2.02
$C_{L\delta e}$	0.6238	0.2724	129

Despite the experimental limitations, wind tunnel studies can provide a useful tool for obtaining a model for an aircraft and validating the model against one determined by theoretical methods. Determining the aerodynamic characteristics using a wind tunnel model of an aircraft is particularly useful for aircraft that have non-conventionally shaped wings, or aircraft that are of more complex designs.

III. MP2028^g Autopilot

In the present project, the Zagi MAV is outfitted with the MP2028^g autopilot[22], designed for fully autonomous operation, from launch to recovery. Figure 2 shows how the autopilot components would be connected when integrated onto the aircraft.

A. Autopilot Components

The MP2028^g has a mass of 74 grams (including servoboard and GPS antenna with co-axial cable), and includes GPS navigation, airspeed hold, altitude hold, and turn coordination. The MP2028^g board itself contains the GPS receiver, microprocessor (for uploading flight and feedback control information), GPS battery, gyros, and sensors. The connector kit provides connectors from the autopilot to the RC receiver. Manual override is also supported, as is data logging. The GPS antenna provided is required to be set on a 3" x 3" copper plane for adequate performance. However, this configuration adds unnecessary weight (the antenna is 27.8 g, and the plate is 42.4 g), and may pose a problem for the aircraft in its flight qualities. An alternate, compatible antenna, the Sarantel 101300, was used instead because it performed equally well (both antennas were used to confirm functionality of the GPS receiver), and at 22.7 g, allows weight conservation. It is also mounted standing up and does not need a copper plane. The autopilot comes with the HORIZON^{mp} software, a user-friendly, graphical interface, to permit mission creation, sensor and servo configuration, parameter adjustment, flight monitoring, and mission simulation. Feedback loop gains and flight parameters may be programmed using the software and uploaded by the user, as well as be adjusted during flight. For the purpose of diagnosing the system or configuring the system indoors, a fake GPS lock was used. The aircraft, though, must not be flown autonomously with a fake GPS lock.

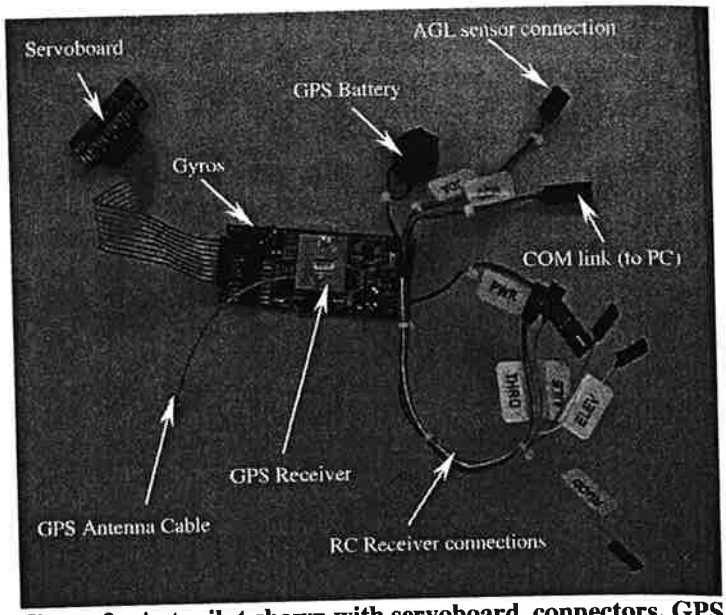

Figure 2. Autopilot shown with servoboard, connectors, GPS connector cable.

Several aircraft configurations are supported by the MP2028^g software (flaps, flaperons, elevons, v-tail, x-tail, split rudders, split ailerons, and flap/aileron mixing), though the simulation is currently restricted to the .40 size RC trainer airframe. Other aircraft/airframe configurations would have to be tested directly in flight. The feedback control loops use PID control, which, in transfer function form, is the following,

$$D(s) = K\left(1 + \frac{1}{T_I s} + T_D s\right) = K + \frac{K_I}{s} + K_D s \tag{1}$$

where K is the proportional gain, and T_I and T_D are the integral and derivative times. Standard control methods were implemented to determine appropriate gains for the closed-loop system to provide adequate stability and performance of the aircraft, and may be found in text books such as Ref. 24.

B. Hardware Integration

Details of the autopilot hardware integration are found in Ref. 23. Power to the autopilot is supplied through the power connector (see Fig. 2) and power to the servoboard is direct. Up to 24 servos may be controlled by the MP2028^g. An external GPS antenna is connected to the integrated GPS receiver via a co-axial cable. Two pressure transducers measure airspeed and altitude. A Pitot tube was attached to the airspeed transducer to obtain airspeed measurements from the dynamic pressure. The altitude transducer measures altitude based on the static air pressure change with altitude change. A COM port allows the MP2028^g to be connected to the serial port of a ground station computer so that the MP2028^g parameters can be set, as well as to download the flight datalog. As is also shown in Fig. 3, a remote control receiver is connected with a select through channel 5 to allow switching between autonomous and pilot-in-control mode. The MP2028^g settings may be changed using either of two programs: the HORIZON^{mp} ground control software (included with the MP2028^g), or HyperTerminal (included with Windows).

IV. Control Design

Several control loops are programmed into the MP2028^g for flight stability and providing navigation capabilities in the autonomous flight mode. For a given airframe, the user may empirically set the PID feedback gains through flight testing, where default values of these gains are provided (located in the aircraft configuration files which can be opened in HORIZON^{mp}) as a starting point. These default values are automatically assigned during the configuration procedure. The aircraft needs to be flown autonomously with a wireless downlink to the ground station PC in order to adjust gains during flight, with gain adjustments made according to the aircraft's response; however, a wireless link was not available at this time. Several of the feedback loop gains may be designed more systematically if the aircraft's characteristics are known. In Table 4, the default gain values are given for the selected feedback loops[22] that PID gains will be designed for, along with a mathematical representation (Laplace transform) of their transfer functions.[23] Methods for determining equations of motion of an aircraft from the stability and control derivatives, are explained in detail in Ref. 18, 19, 24, and 25 and a control design using the derived transfer functions is shown using the elevator-from-pitch feedback loop as an example.

Table 5 shows the factors[26] needed in order to convert the gain values used by the MP2028^g to gain values that could be tested in simulation software (MATLAB®, Simulink®, etc.).[27,28] The first column is an identifier number used by the autopilot processor for that specific feedback loop. Associated with each feedback loop is a sampling rate, at which the closed-loop system reads the input data, and it must be considered, along with several factors such as rate limits, etc., in the control design.

Table 4: Feedback Loop Gains of MP2028g.[22]

Feedback loop	Transfer Function	Proportional Gain	Integral Gain	Derivative Gain
Aileron from Roll	$\frac{\phi(s)}{\delta_a(s)}$	-75000	-128	-3000
Elevator from Pitch	$\frac{\theta(s)}{\delta_e(s)}$	16000	9800	8900
Pitch from Altitude	$\frac{h(s)}{\theta(s)} = \frac{U_o}{s}\frac{\gamma(s)}{\theta(s)}$	320	353	800
Pitch from Airspeed	$\frac{u(s)}{\theta(s)}$	13756	24	194
Roll from Heading	$\frac{\psi(s)}{\phi(s)} = \frac{g}{U_o s}$	-200	0	-50
Pitch from Descent Rate	$\frac{\dot{h}(s)}{\theta(s)} = U_o\frac{\gamma(s)}{\theta(s)}$	-1500	-150	-1719

Table 5: Gain Conversion Factors for PID Feedback Control.[26]

	Feedback Loop		Divisor		Input units	Output units
0	Aileron From Roll (30 Hz)	P	12	4096	Radians times 1024	Fine servo
		I	15	32768		
		D	8	256	Rads per second times 1024 times 21	
1	Elevator From Pitch (30Hz)	P	9	512	Radians times 1024	Fine servo
		I	14	16384		
		D	11	2048	Rads per second times 1024 times 21	
		DD	10	1024	Rads times 1024	
6	Pitch from altitude (5Hz)	P	10	1024	Feet times 8	Radians times 1024
		I	15	32768		
		D	10	1024	Feet per second	
8	Pitch from airspeed (5Hz)	P	10	1024	Feet per second	Radians times 1024
		I	10	1024		
		D	8	256	Feet per second squared	
9	Roll from Heading (5Hz)	P	13	8192	Degrees times 100	Radians times 1024
		I	10	1024		
		D	10	1024	Degrees times 100 per second	
14	Pitch from descent rate (5Hz)	P	10	1024	Feet per second	Radians times 1024
		I	15	32768		
		D	10	1024	Feet per second squared	

Each gain is split into a multiplier and a divisor to allow integer math for the autopilot to calculate the feedback loops. The gain value visible in the configuration file is the multiplier (this is the number changed when the gain is adjusted). The complete gain is the multiplier divided by the divisor. The first column of the divisor column in Table 5 is the number of bits shifted when the division is applied, and the equivalent divisor (second column) is $2^{\text{no. of bits shifted}}$. To complete the gain conversion, it is necessary to also divide by the given input units' multiplying factor. As an example, the default proportional gain for the elevator-from-pitch feedback loop may be found by the following conversion,

$$K = \frac{K_{MP2028}}{Divisor * 1024} = \frac{16000}{512 * 1024} = 0.0305$$

Proceeding in a similar manner and using the definitions for each gain, we can convert all the gains for simulation purposes in MATLAB®. The converted gains are summarized in Table 6.

Table 6: Converted Feedback Loop Gains of MP2028[g].

Feedback loop	Transfer Function	Proportional Gain	Integral Time	Derivative Time
Aileron from Roll	$\frac{\phi(s)}{\delta_a(s)}$	-0.01788	4685.99	0.03048
Elevator from Pitch	$\frac{\theta(s)}{\delta_e(s)}$	0.0305	52.214	0.0066
Pitch from Altitude	$\frac{h(s)}{\theta(s)} = \frac{U_o}{s}\frac{\gamma(s)}{\theta(s)}$	0.0119	28.993	20.0105
Pitch from Airspeed	$\frac{u(s)}{\theta(s)}$	4.0946	573.1724	0.0564
Roll from Heading	$\frac{\psi(s)}{\phi(s)} = \frac{g}{U_o s}$	-0.0140	∞	2
Pitch from Descent Rate	$\frac{\dot{h}(s)}{\theta(s)} = U_o\frac{\gamma(s)}{\theta(s)}$	-0.4465	320.0112	1.146

The pitch-from-elevator loop will be used as an example for designing feedback loop gains. Using the properties of Tables 1 and 2 and a steady state velocity of U_o = 20 m/s, with the aircraft at steady, level flight, the resulting elevator-from-pitch transfer function is the following,[23]

$$\frac{\theta(s)}{\delta_e(s)} = \frac{-13482.974s^2 - 219201.910s - 208004.227}{20s^4 + 690.171s^3 + 27641.258s^2 + 8612.602s + 30915.224} \quad (2)$$

For this transfer function, the zero-frequency gain (s = 0) is -6.7282. Consequently, a positive input to the elevon will result in a negative pitch response, as would be expected (a downward deflection of the elevon is positive by convention). One of the easiest ways to determine gains for the PID controller is to use a root-locus plot. The root-locus plot for the elevator-from-pitch transfer function (Eq. 2) is shown in Fig. 5, with a suitable design gain for a proportional feedback loop. Both positive and negative gain behavior is shown for completion.

Note how it was necessary to use a negative gain for the feedback control. In the closed-loop system, a reference pitch will be read by the control law and will compare it to the response pitch. In order to produce a response that will reduce the error at steady state, the control command will require the opposite sign to obtain the desired pitch. By making the gain larger and negative, the two short period poles are pushed asymptotically towards the imaginary axis, while the two phugoid poles move away from the imaginary axis within the left half plane and towards the two zeros. Note also from Table 4 that the gains were originally programmed with positive signs for this loop. When the gains are designed and converted for use in the MP2028^g, the signs will have to be changed from negative to positive. Once the proportional gain is determined, the integral and derivative terms of the control law are added (in the forward loop), and additional root-locus plots are created to determine the influence of the additional poles and zeros of the control law on the closed-loop system. The integral gain K_I (through T_I) and derivative gain K_D (through T_D) are adjusted to place the poles and zeros accordingly. Continuing with the design to produced a closed-loop system with a quick response and low steady-state errors, the following values were determined for each of the three parameters: K_P = -0.5, T_I = 1, and T_D = 0.01. Converting back to gains for use in the MP2028, the proportional, integral, and derivative gains are: K_P = 262144, K_I = 8388608, and K_D = 220201 (as they would be entered in the MP2028^g). The root-locus plot for the PID compensated system is shown in Fig. 6.

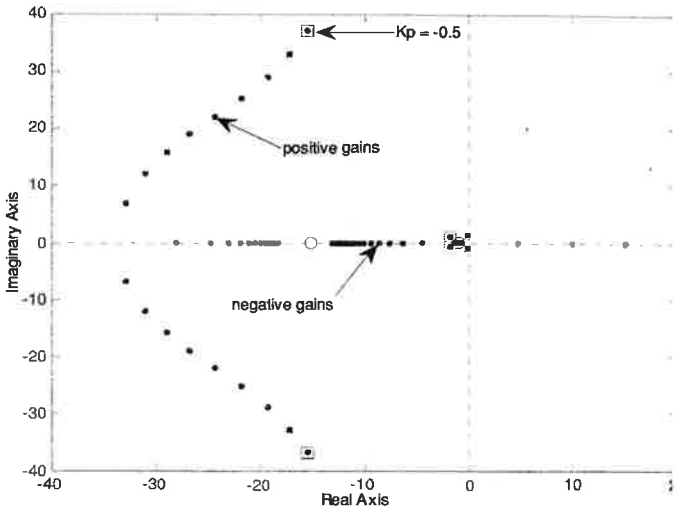

Figure 5. Root-locus plot for elevator-from-pitch.

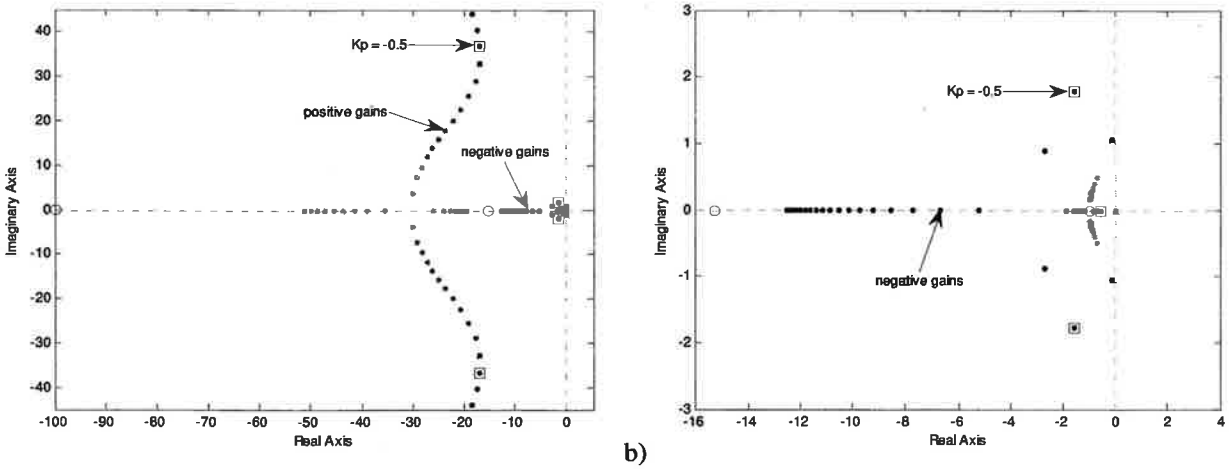

a) b)

Figure 6. a) Root-locus plot for elevator-from-pitch with PID control. b) Magnified view of phugoid pole behavior.

The PID controller used in the forward loop will add a zero at -100 from the T_D term (see Fig. 6a), an additional zero at -1 from the T_I term, and a pole at the origin. Now, as the closed-loop system gain is increased in the negative direction, the short period poles will eventually collide near -197 on the real axis, with one pole moving to the zero at -100, and the other moving to infinity. The phugoid poles will also collide on the negative real axis, with one moving to the zero at -15.25, and the other to the zero at -1.01. The pole at the origin will move towards the zero at -1. Had a positive gain been used, the system will certainly be unstable, since the pole at the origin will move along

the positive real axis. Figure 6b shows in greater detail the portion of the root-locus plot involving the phugoid poles and the pole at the origin.

Finally, the time response of the closed-loop system is shown in Fig. 7, simulated at the 30 Hz sampling rate used by this feedback loop. A reference pitch of 5 degrees is used here. The system responds well, settling within ~5 seconds, and exhibits a ~10 percent overshoot initially (an acceptable response).

Using the above procedure, the PID control can be designed by simply placing the system poles appropriately through gain selection to obtain a stable, closed-loop system. The controller can then be tested to verify the time response of the system and tuned to improve the system response. A relatively quick response to a step reference input is desired, while limiting the overshoot to an acceptable level. A summary of all the design gains for the various feedback loops are given in Table 7.

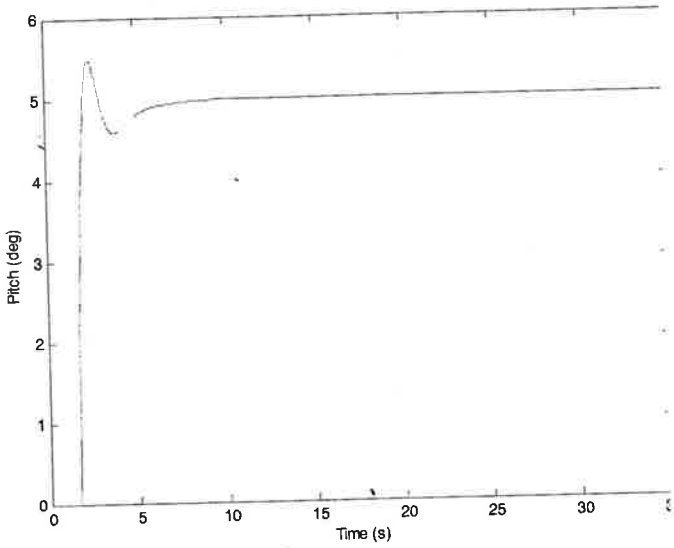

Figure 7. Elevator-from-pitch response with PID compensation to a 5 degree reference pitch.

Table 7: Designed Feedback Loop Gains of MP2028[g].

Feedback loop	Proportional Gain	Integral Time	Derivative Time
Aileron from Roll	-2936	-93952	-117
Elevator from Pitch	262144	8388608	220201
Pitch from Altitude	806	1518	0
Pitch from Airspeed	4031	5039	0
Roll from Heading	-14298	0	-9
Pitch from Descent Rate	-1500	-9600	0

The feedback loops that use the pitch attitude as the "control input" are the altitude, airspeed, and descent rate loops. During level flight, the pitch attitude is used to control the aircraft altitude. For the Zagi, the following transfer function results for a 20 m/s cruise speed,[23]

$$\frac{h(s)}{\theta(s)} = \frac{580.875s^3 - 15834.059s^2 - 4423382.856s - 3628352.308}{-13482.974s^3 - 219201.910s^2 - 208004.227s} \quad (3)$$

This particular feedback loop can be controlled using a coupler (a PI control).[25] The integral gain provides a weighting factor to keep the aircraft on a desired flight path angle in the midst of disturbances (i.e., turbulence, etc.). Figure 12 shows a block diagram for an arrangement for the altitude control using pitch attitude closed-loop control system (developed from the elevator-from-pitch transfer function) in the open-loop so that the pitch response is fed directly to the pitch-from-altitude transfer function.

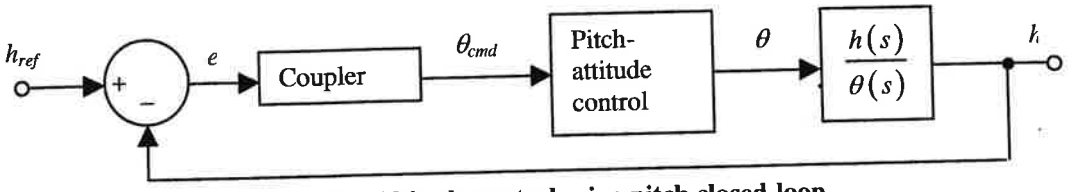

Figure 8. Altitude control using pitch closed-loop.

The pitch is used to control the descent rate as well. The pitch attitude control closed-loop system, derived from the elevator-from-pitch feedback loop, was incorporated in the forward loop. The result is the following open-loop transfer function,

$$\frac{\dot{h}(s)}{\theta(s)} = \frac{\theta(s)}{\theta_{cmd}(s)} \cdot \frac{580.875s^3 - 15834.059s^2 - 4423382.856s - 3628352.308}{-13482.974s^2 - 219201.910s - 208004.227} \tag{4}$$

Similar to the pitch-from-altitude transfer function, a PI control may be used to control the closed-loop system.

V. Flight Testing of 36-inch Zagi with MP2028[g]

Flight tests were performed on the Zagi MAV to evaluate overall flight qualities and to test equipment functionality. Also, trim adjustments could be made during flight, while response to control input, as well as external disturbances could be observed.

A. Remote Controlled Flight

A sample of the flight data for the aircraft in remote control mode is presented here. GPS functionality was not available during this set of tests. During the flight test, the aircraft was subject to large wind speeds and gusts, as well as mechanical vibrations from the motor itself. As the large amount of wind provided significant, unavoidable, external influence on the Zagi's motion, the response of the aircraft shown is not entirely due to the manual control inputs.

Figures 9-11 show the pitch, roll, and yaw angle response of the Zagi MAV to manual control surface inputs over a small range of the flight test. The aircraft was hand launched and the motor turned on at the 300 second mark. The wind conditions made it difficult to maintain the aircraft in trim, and constant input to the control surfaces was necessary to maintain level flight. Note that where the control surface deflections are in the same direction, the control input is pure elevator, and opposite deflections pure aileron. The control surface channel connections are such that aileron deflection is measured from the left control surface, while the elevator deflection is measured from the right control surface. It can be seen from Fig. 9, for example, at a time of 445 seconds, that elevator input was imparted from the remote control, causing the aircraft to pitch.

During flight, trim adjustments had to be made constantly due to a slight drag and slight weight bias to the right because of equipment positioning (antenna, etc.) on the right wing (thus the negative aileron setting ~-3-6 deg). Placing the antenna out on the wing keeps the antenna isolated from the electronics at the center of the aircraft, thus minimizing interference from the rest of the electronics (this will be necessary when GPS signals are needed for autonomous flight). Some of the flight stretch shown in Fig. 9 shows normal behavior in the pitch gyro measurement, though some cases of extreme motion are also indicated (but not actually observed during the flight). This could be due to the extreme flight conditions and motor vibrations that the gyros and sensors are being subject to, causing the gyros to "spin" and show the aircraft to be "looping", which it rarely did. The small size of the Zagi limits the placement of the autopilot electronics, thus limiting vibration isolation for the electronic equipment and sensors. In Fig. 10, the roll response overall shows the aircraft to bias towards a right roll for the reasons stated above, thus requiring constant left trim correction. As with the pitch motion, some extreme motion is shown in the data, though these types of incidences, such as full rollover, were not observed as frequently during flight as the data indicates. In general, though, a positive aileron deflection caused the aircraft to roll in the positive direction. Finally, Fig. 11 shows the yawing motion of the aircraft due to control surfaces. Some extreme motion was

recorded by the gyro sensors again (but not observed in so many instances in flight). In general, positive aileron input resulted in a positive yaw angle.

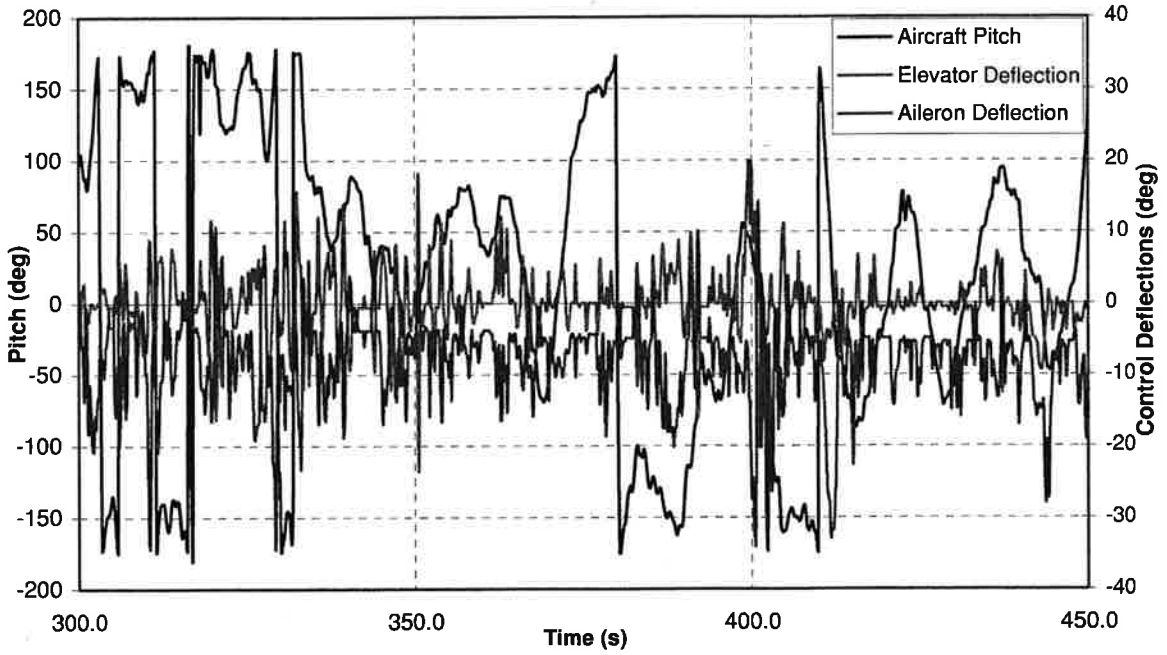

Figure 9. Pitch attitude of Zagi and control surface deflections.

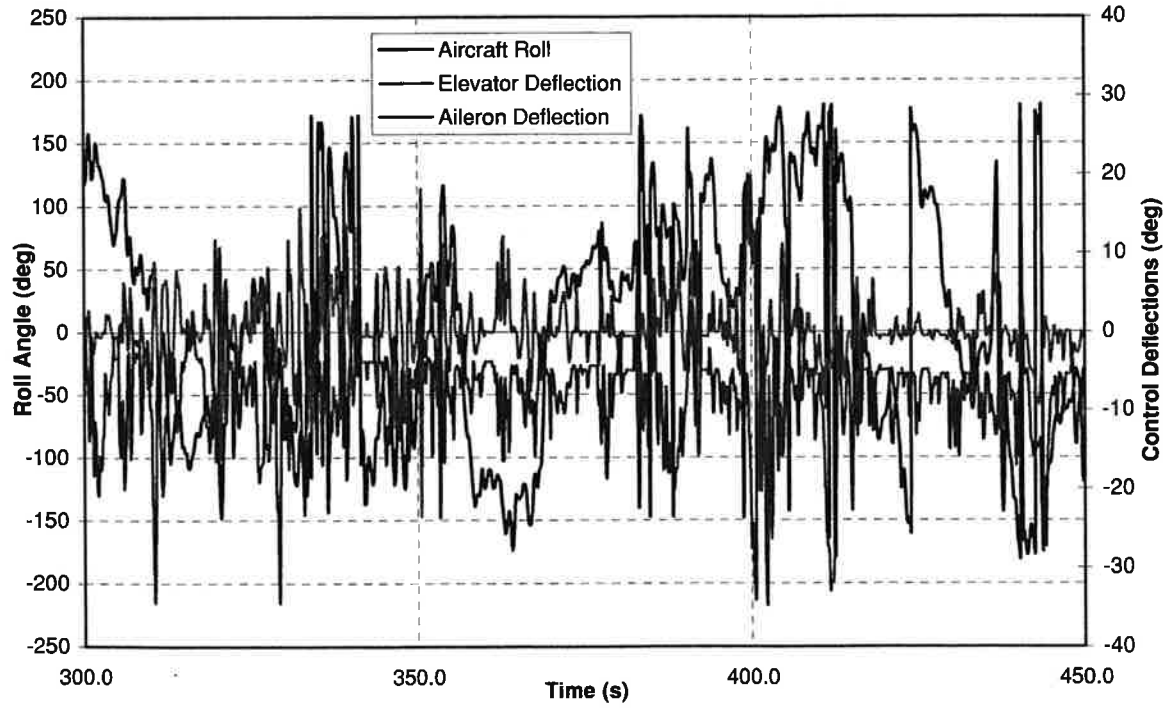

Figure 10. Rolling motion of Zagi and control surface deflections.

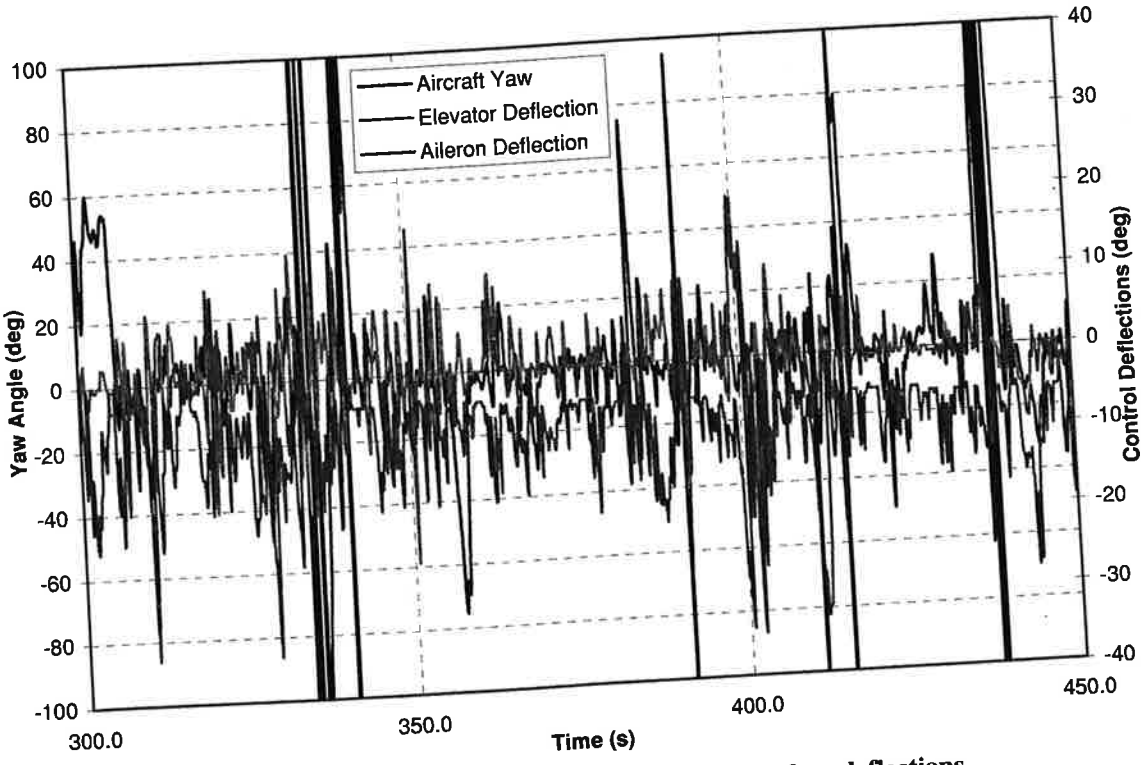

Figure 11. Yawing motion of Zagi and control surface deflections.

B. Ground Testing in Autonomous Mode

Figure 12 shows ground test results with the autopilot set to autonomous mode, with results obtained when a true GPS lock was available, showing the control surface behavior for a given pitch. Similar observations were made for roll and yaw displacements. While the autopilot was connected to the ground station through the COM connection, a take-off was initiated from the HORIZON^{mp} interface (the propeller was removed from the motor for safety). By hand, the aircraft was moved (to simulate disturbances) to verify control actuation. As was expected, the control surfaces moved to "oppose" the motion.

Since the aircraft does not have any means to directly control pure yaw disturbances (normally, that would be done by a rudder), the elevons did not deflect very much (up to ~5 degrees) to oppose pure yaw motion. Also, without a control surface to directly control heading, the autopilot has to indirectly control heading from roll, with the roll angle as an "input" (i.e., the autopilot uses the roll-from-heading feedback loop to determine the required roll, and then the aileron deflection is determined using the aileron-from-roll feedback loop). If a wireless modem connection is available for the COM connection, the aircraft could be launched with assistance before a take-off command is issued, after which the aircraft should follow a predetermined flight plan when in autonomous mode.

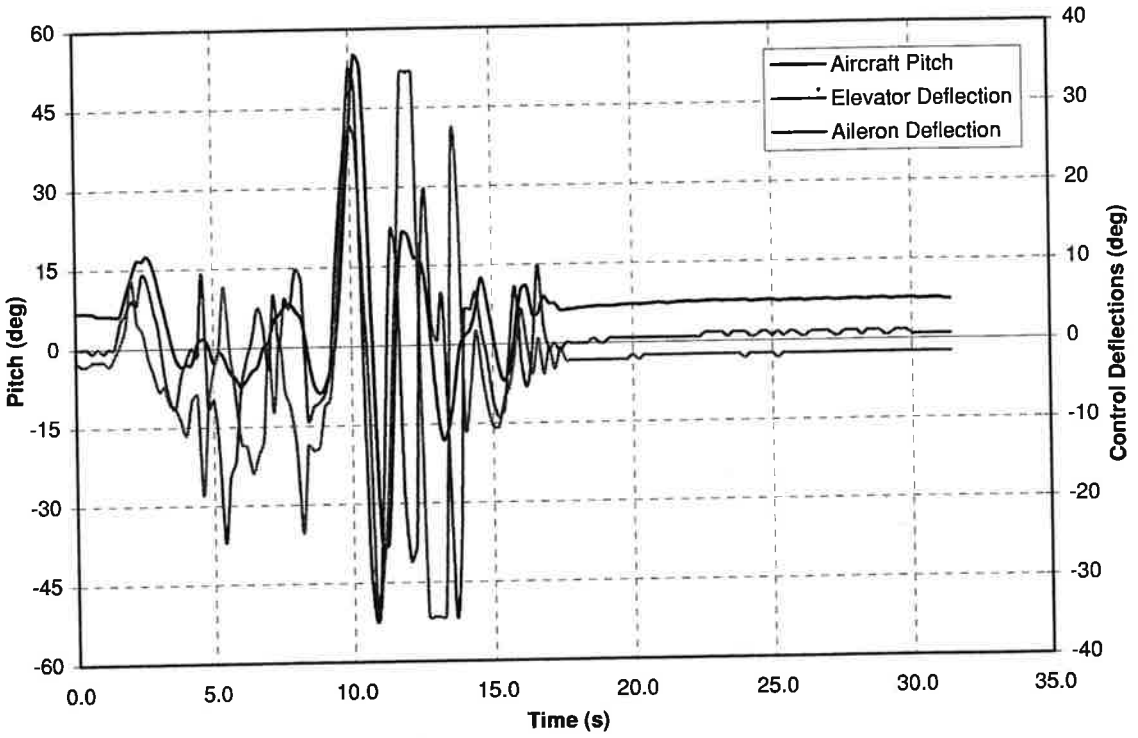

Figure 12. Control surface response to pitching motion for aircraft in autonomous mode.

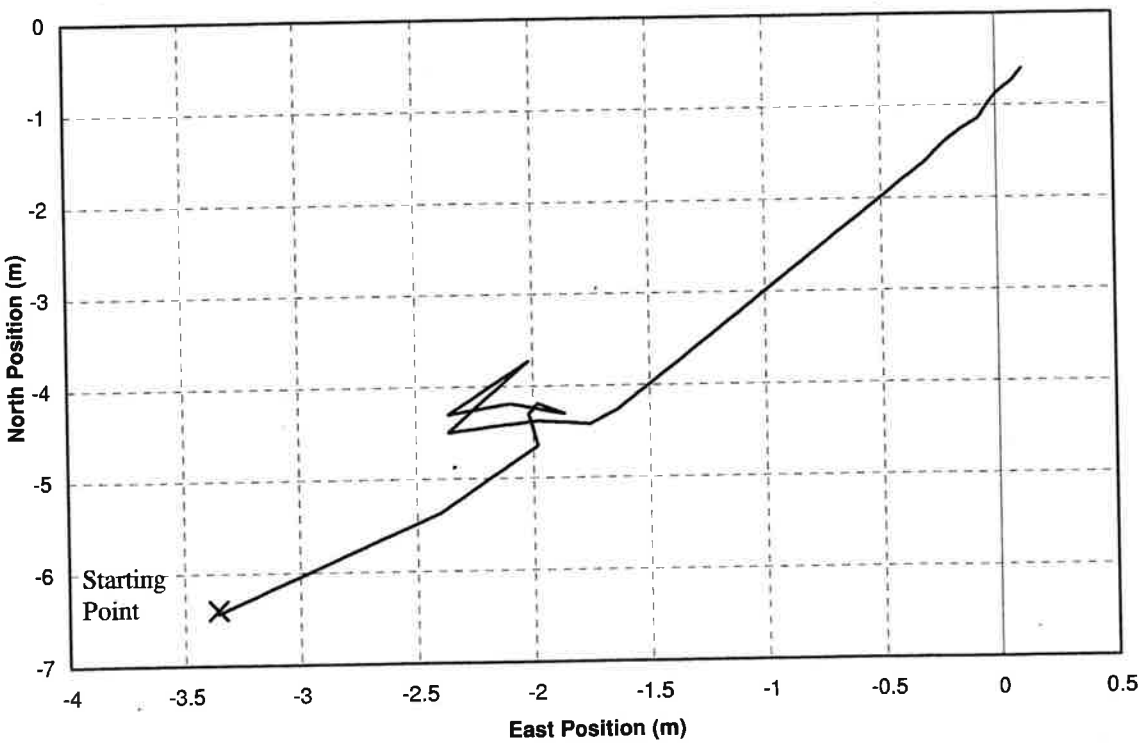

Figure 13. Position of aircraft recorded by GPS system during ground test.

Figure 13 shows ground position data that was recorded by the GPS system. During autonomous flight, the aircraft's path can be traced out and validated against the flight plan for accuracy. The starting point is offset from (0,0) by ~6.5 m South and 3.5 m West, giving an indication of the accuracy of the GPS system. As such, if a waypoint in the flight plan is located 100 m North of the starting point, its actual location could be within 6.5 m of that location along the north-south direction. GPS positioning errors will vary with availability and positioning of satellites. To help overcome uncertainties in the GPS positioning, a waypoint circle diameter can be set. This circle is what the aircraft has to enter so that the autopilot can register that a waypoint has been reached/passed.

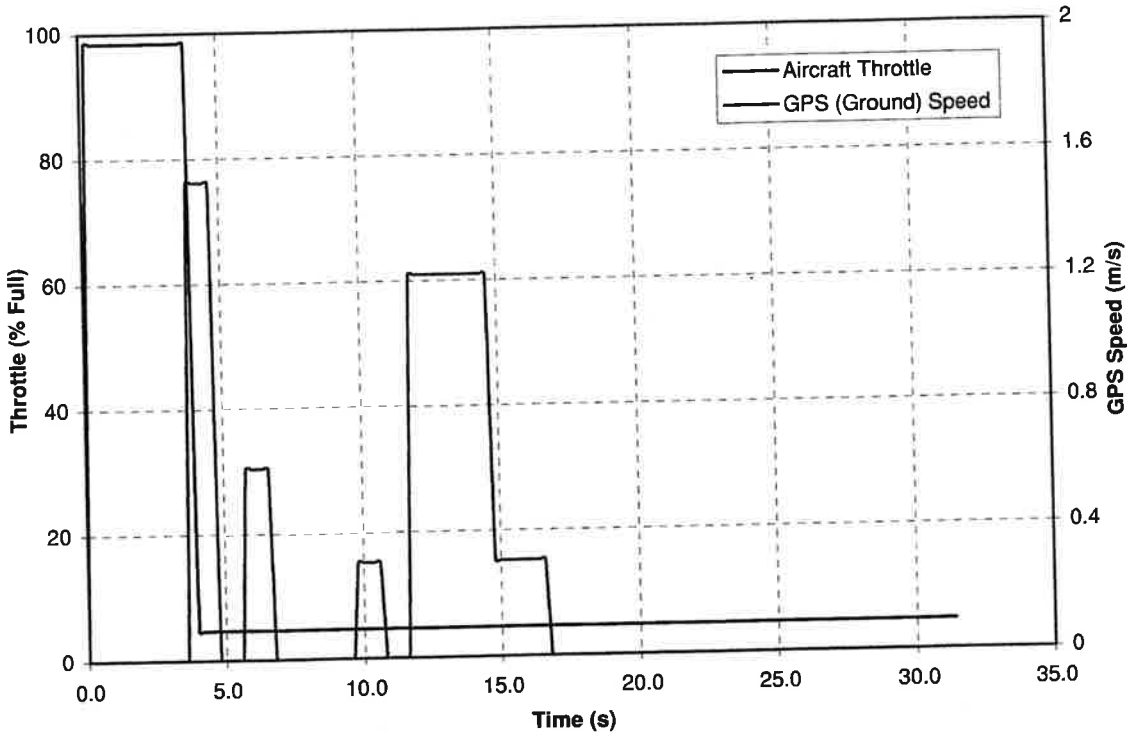

Figure 14. GPS speed and throttle during ground test in autonomous mode.

In Fig. 14, data recorded for throttle position and GPS speed (speed relative to the ground) is shown during ground testing in autonomous mode, with the aircraft being moved around by hand to generate GPS readings. When a take-off was initiated, the throttle briefly operated at its maximum setting, but shut off after about 4 seconds. It is expected that the throttle would continue to operate, but GPS speed was not recorded during this interval, as indicated by the plot. The autopilot did not sense that there was any motion, nor that the aircraft was actually headed to its first waypoint, and shut off the motor (which should not be the case during fully autonomous flight). After that, the GPS system sensed speed at rather sporadic intervals, suggesting that a GPS lock was not being maintained consistently.

Further ground testing was performed to determine appropriate positioning of the antenna closer to the fuselage (to avoid causing added drag from the antenna over the wing, otherwise requiring larger than normal trim adjustments in the opposite direction) and still allow the antenna to acquire a GPS signal while limiting interference between the antenna, the autopilot, and other electrical components. Interference between the antenna and the rest of the electronics may cause the antenna to acquire more slowly, not at all, or the GPS signal is more likely to be lost in flight. Due to an unexpected failure of the autopilot during a ground test over the last days of the project, autonomous flight testing could not be undertaken.

VI. Concluding Remarks

A methodology for systematically designing PID control gains for the MP2028^g autopilot was presented. First, a model of the 36-inch Zagi was developed using analytical methods, including the use of an evaluation version of the Advanced Aircraft Analysis (AAA) software available from DARCorp. The stability and control derivative coefficients were determined and compared with results from wind tunnel experiments. A scaled model of the aircraft was developed and flight conditions were replicated in wind tunnel tests by matching low speed chord Reynolds numbers. With the model aircraft not expected to fly faster than 20 m/s, Mach number and compressibility effects were neglected. Sensitivity issues did not permit accurate measurements of many of the aerodynamic coefficients, especially those that have small values.

Using the values of the stability and control derivatives, the linear, perturbed equations of motion were formed and the six standard transfer functions were determined for both the longitudinal and lateral-directional degrees of freedom, as well as transfer functions for the additional control and navigation feedback control loops needed. Proportional, Integral, and Derivative (PID) control gains were determined using root-locus analysis/pole-placement techniques. Time simulations were used to evaluate the suitability of the chosen gains according to response speed and overshoot, and to ensure stability for the required sampling frequencies.

During remote control flight tests, measurements from the roll, pitch, and yaw gyros showed instances of extreme motion (looping, full rolls, and overall large angular motion) during flight, but not actually observed. As the aircraft responded quickly to control inputs and wind gusts, the gyros did not have time to settle between maneuvers or external disturbances. Also, with the motor in close proximity to the autopilot, the gyros were subject to vibrations due to the motor's operation. The small size of the Zagi limited the placement of the autopilot electronics, thus vibration isolation for the electronic equipment and sensors is limited. Ground tests of the gyros and sensors, though, under more controlled conditions did not reveal any problems. Since the feedback loops require reliable measurements from the gyros, autonomous flight with the autopilot for the 36-inch Zagi would be difficult.

Ground tests were performed with the autopilot in autonomous mode to evaluate functionality of control response and GPS data acquisition, as well as determine the approximate amount of error in GPS positioning. The aircraft showed the expected control response to oppose roll, pitch, and yaw motion that may be caused by external disturbances during flight. Also, it was possible to record the aircraft's path from the GPS positioning data. An attempt to reposition the GPS antenna closer to the fuselage instead of out on the wing was made to overcome weight distribution and drag bias; however, the drawback of the new arrangement is possible interference from the rest of the autopilot electronics, thus reducing the functionality of the antenna. Methods will need to be developed to provide better isolation between the antenna and the rest of the electronics. An unexpected failure of the autopilot during the ground test prevented autonomous flight from taking place.

References

1. McMichael, J. M. and Francis, M.S., "Micro Air Vehicles – Toward a New Dimension in Flight," TTO document, August 7, 1997. Internet source: http://www.darpa.mil/tto/mav/mav_auvsi.html. [Cited Jan. 31st, 2005].

2. Null, W. and Shkarayev, S., "Effect of Camber on the Aerodynamics of Adaptive wing Micro Air Vehicles," *2nd AIAA Flow Control Conference*, June 28 – July 1, 2004, Portland, OR. AIAA-2004-2694.

3. Shkarayev, S., Null, W., and Wagner, M., "Development of Micro Air Vehicle Technology with In-Flight adaptive-Wing Structure," NASA/CR-2004-213271, October 2004.

4. Null, W., "The Design and Development of an Adaptive Wing Micro Air Vehicle," M.S. thesis, University of Arizona, 2003.

5. Waszak, M. R.; Jenkins, L. N., and Ifju, P., "Stability and Control Properties of an Aeroelastic Fixed Wing Micro Aerial Vehicle," *AIAA Atmospheric Flight Mechanics Conference*, August 6-9, 2001, Montreal, Canada. AIAA-2001-4005.

6. Ifju, P. G., Jenkins, D. A., Ettinger, S., Lian, Y., Shyy, W., and Waszak, M. R., "Flexible-Wing-Based Micro Aerial Vehicles," *40th AIAA Aerospace Sciences Meeting and Exhibit*, January 14-17, 2002, Reno, NV. AIAA-2002-0705.

7. Foster, T. M., and Bowman, W. J., "Dynamic Stability and Handling Qualities of Small Unmanned-Aerial-Vehicles," *43rd AIAA Aerospace Sciences Meeting and Exhibit*, January 10-13, 2005, Reno, NV. AIAA-2005-1023.

8. Hsiao, F., Chien, Y., Liu, T., Lee, M., Chang, W., Han, S., and Wang, Y., "A Novel Unmanned Aerial Vehicle System with Autonomous flight and Auto-Lockup Capability," *43rd AIAA Aerospace Sciences Meeting and Exhibit*, January 10-13, 2005, Reno, NV. AIAA-2005-1050.

9. Arning, R. K. and Sassen, S., "Flight Control of Micro Aerial Vehicles," *AIAA Guidance, Navigation, and Control Conference and Exhibit*, August 16-19, 2004, Providence, RI. AIAA 2004-4911.

10. Taylor, B., Bil, C., Watkins, S., "Horizon Sensing Attitude Stabilisation: A VMC Autopilot," *18th International UAV Systems Conference*, Bristol, UK, 2003.

11. Gad-el-Hak, M., "Micro-Air-Vehicles: Can They Be Controlled Better?" *Journal of Aircraft*, Vol. 38, No. 3, 2001, pp. 419-429.

12. Flake, J., Frischknecht, B., Hansen, S., Knoebel, N., Ostler, J., and Tuley, B., "Development of the Stableyes Unmanned Air Vehicle," *8th International Micro Air Vehicle Competition*, 2004, University of Arizona, Tucson, AZ.

13. Quix, H., "Design of an Autonomous Micro Air Vehicle," *8th International Micro Air Vehicle Competition*, 2004, University of Arizona, Tucson, AZ.

14. Chung, D.K., Ryu, J.H., Nam, I.C., Jo, K.Y., Yoon, K.J., Huang, H.C., and Kim, J.H., "Development of Fixed Wing MAV "Batwing" at Konkuk University," *9th International Micro Air Vehicle Competition*, 2005, Konkuk University, Seoul, South Korea.

15. *Pico-Pilot Miniature Digital Flight Control for Unmanned Air Vehicles.* User's Manual, rev 1.08.

16. Trick R/C, 2004. Internet Source: http://www.zagi.com. [Cited May 31st, 2005].

17. College of Science & Technology, Nihon University, *NASG Airfoil Database.* Internet Source: http://www.nasg.com/afdb/show-polar-e.phtml?id=441. [Cited May 31st, 2005].

18. Roskam, J., *Airplane Flight Dynamics and Automatic Flight Controls, Part I*, Design, Analysis and Research Corporation (DARCorp), 1998.

19. Roskam, J., *Methods for Estimating Stability and Control Derivatives of Conventional Subsonic Airplanes*, Roskam Aviation and Engineering Corporation, 1983.

20. Design, Analysis, and Research Corporation, 1991. Internet Source: http://www.darcorp.com. [Cited May 31st, 2005].

21. Wagner, M., "Design and Performance Analysis of a Micro Air Vehicle," M.S. thesis, University of Arizona, 2002.

22. *MicroPilot MP2028g Installation and Operation.* 2001, MicroPilot.

23. Platanitis, G. and Shkarayev, S., "Integration of an Autopilot for a Micro Air Vehicle," NASA Report, June 2005.

24. Franklin, G. F., Powel, J. D., and Emami-Naeini, A., *Feedback Control of Dynamic Systems.* Addison-Wesley Publishing Company, Inc., 1994, Third Edition.

25. Roskam, J., *Airplane Flight Dynamics and Automatic Flight Controls, Part II*, Design, Analysis and Research Corporation (DARCorp), 1998.

26. Technical correspondence with MicroPilot support staff.

27. *Control System Toolbox, User's Guide, Version 6*, The MathWorks, Inc., 2005.

28. *Simulink Control Design, Version 1*, The MathWorks, Inc., 2005.